



Flow regimes and dynamic similarity of immersed granular collapse: A CFD-DEM investigation

L. Jing^a, G.C. Yang^b, C.Y. Kwok^{a,*}, Y.D. Sobral^b

^a Department of Civil Engineering, The University of Hong Kong, Pokfulam Road, Hong Kong, China

^b Departamento de Matemática, Universidade de Brasília, Campus Universitário Darcy Ribeiro, 70910-900 Brasília, DF, Brazil

ARTICLE INFO

Article history:

Received 24 October 2018

Received in revised form 3 January 2019

Accepted 13 January 2019

Available online 18 January 2019

Keywords:

CFD-DEM

Granular collapse

Immersed granular flow

Flow regime

Scaling law 2010 MSC: 00-01

99-00

ABSTRACT

Immersed granular collapses may encounter different flow regimes, such as free-fall (dry), fluid-inertial, and viscous regimes, depending on column geometry, particle size, particle density, fluid viscosity, and many other parameters. Understanding the controlling parameters of these regimes is important for both industrial and geological applications where grains and fluids coexist. It is also important to combine these parameters into dimensionless groups to guide down-scaled experiments and numerical simulations. In this work, we derive a set of dimensionless numbers (i.e., Stokes number, density ratio, and Reynolds number) based on typical time scales in the sedimentation of a sphere, and successfully verify the relevance of these numbers in determining flow regimes and maintaining dynamic similitude across length scales. The numerical method we use couples the computational fluid dynamics and discrete element method (CFD-DEM), which allows a wide variety of particle size and fluid viscosity to be chosen, keeping constant the Stokes number and density ratio. Quantitative data of front propagation and energy evolution are presented to characterize flow dynamics in different flow regimes. The collapse exhibits a transition from sliding-dominant to suspension-dominant behaviors as the Stokes number decreases, which gives rise to distinct deposit morphology in different regimes. Our findings enhance the understanding of inertial and viscous behaviors of immersed granular flows. The verified scaling rules and dimensionless parameters are of potential use in small-scale experiments and simulations where appropriate scaling is essential.

© 2019 Elsevier B.V. All rights reserved.

1. Introduction

Granular flows in fluids, or immersed granular flows, are ubiquitous not just in industrial applications such as pharmaceutical production, chemical engineering, and food production [1,2], but also in environmental problems including submarine landslides and sediment transport [3,4]. In the study of immersed granular flows, the collapse of granular columns has received much attention as a test model due to its simple configuration but rich (and unsteady) behaviors [5–9]. In a column collapse test, an initial granular mass is suddenly put into motion by gravity, which then spreads and deposits over a certain runout distance. In collapses where the influence of the ambient fluid is negligible (i.e., dry granular collapse), the initial aspect ratio of the column is known to be the major controlling parameter of the final runout [10–13].

When the ambient fluid plays a role (i.e., immersed granular collapse), more complicated behaviors that are not relevant in dry cases may emerge, depending on the types of grains and fluids. As such, relevant parameters for the immersed problem may include the aspect

ratio, grain size, packing density, and fluid viscosity. For instance, our recent work [9] reported a significant fluid-inertial effect (i.e., fluid eddies erode the surface of the granular deposit) in underwater granular collapses especially when the initial aspect ratio is high. By varying particle size, an earlier study [7] found that the collapse dynamics of an underwater column consisting of coarse grains is mainly described by the balance between horizontal pressure gradient and Coulomb friction, while for finer particles, hydrodynamic fluid pressure and drag forces become dominant, leading to dense-suspended granular flows. Regarding packing density, a series of laboratory experiments [6] showed that variation of the initial packing density can give rise to significantly different flow regimes for immersed granular collapses. In particular, the collapse of a densely-packed column is much delayed by the negative excess pore pressure generated during the dilation of the granular skeleton, while a loose packing leads to fast dynamics due to the development of positive excess pore pressure during contraction [6]. Such evolutions of excess pore pressure resulting from dense and loose packings were presented with more details in a numerical study [14]. For the effect of fluid viscosity, numerical simulations with a coupled fluid-particle method [8] showed that the mobility of particles may be largely enhanced by contact lubrication in the fluid-inertial regime, and a transition from inertial to viscous regimes occurs as fluid viscosity increases.

* Corresponding author.

E-mail address: fiona.kwok@hku.hk (C.Y. Kwok).

It remains a challenge to give a full picture of the flow regimes encountered by immersed granular flows. Three distinct flow regimes have been reported previously in granular avalanches [15,16], namely, the free-fall (grain-inertial), fluid-inertial, and viscous regimes, for which two dimensionless numbers, i.e., the Stokes number [15] and the particle-fluid density ratio, are proposed to be the controlling parameters. In recent studies of granular and suspension rheology [17,18], a viscoinertial number is proposed to combine the inertial number [19,20] and viscous number [17] that control the dynamics of granular flows in dry and suspension regimes, respectively. While the aforementioned findings were mainly established with the configuration of periodic or steady granular flows, the flow regimes in a transient granular system (such as the granular collapse problem to be addressed in this work) are still poorly characterized, especially in terms of relevant dimensionless numbers.¹ As one of the limited studies in the literature, Topin et al. [8] found grain-inertial, fluid-inertial, and viscous regimes when simulating granular collapses in air, water, and a more viscous fluid, respectively.

The aim of the current work is to characterize the flow dynamics of granular collapses in a variety of regimes and, more importantly, to find a set of dimensionless numbers that govern the different behaviors of immersed granular flows. To this end, we derive different dimensionless numbers based on the typical time scales related to the motion of a single sedimenting sphere in a fluid, inspired by a few previous studies [15,22], and perform a series of test cases with coupled continuum-discrete simulations to verify the relevance of these dimensionless numbers against the collective dynamics of the more complicated granular system.

The paper is organized as follows. In Section 2, we describe the formulation of the relevant time scales and dimensionless numbers as the theoretical background. In Section 3, we present the details of our numerical method, model setup, and test plan. The results are presented and discussed in Section 4. Conclusions are drawn in Section 5.

2. Theoretical background

This section provides theoretical background for our analysis. We first present different flow regimes encountered by a sedimenting sphere and derive the dominant time scale for each regime (Section 2.1). The time scales are then used to formulate major dimensionless numbers in Section 2.2. In Section 2.3, we describe the scaling of particle contact parameters in a simple collision scenario.

2.1. Time scales in different flow regimes

We start with a simple elementary scenario, i.e., the sedimentation of a single particle in a fluid. The motion of the particle is governed by

$$\frac{\pi}{6}d_p^3\rho_p\frac{dv}{dt} = \frac{\pi}{6}d_p^3\Delta\rho g - F_d \quad (1)$$

where v is particle velocity, d_p is particle diameter, ρ_p is particle density, $\Delta\rho = \rho_p - \rho_f$ is the density difference between the particle and fluid, with ρ_f being fluid density, g is the gravitational acceleration, and F_d is drag force. The first term on the right-hand side represents a combination of gravity and buoyancy forces (or, the buoyant weight). The drag force, F_d , may take different forms for different flow regimes [23]. In the following, we discuss three distinct regimes, namely, the free-fall (dry), viscous, and inertial regimes, which are respectively denoted by letters F, V, and I in the notation.

¹ After completion of this work, we become aware of a recent research article [21] that presents a similar idea of using dimensionless numbers to explore the flow regimes of immersed granular collapses. We give a more detailed discussion on this work in Section 4.5.

2.1.1. Free-fall regime

In the free-fall regime, which typically refers to dry cases, drag force is negligible ($F_d \approx 0$). By solving Eq. (1), one can easily obtain a characteristic time

$$\tau_F = \sqrt{\frac{2\rho_p d_p}{\Delta\rho g}} = \sqrt{\frac{2d_p}{g'}} \quad (2)$$

which is the time for the particle to travel a distance of d_p from rest. For generality, we do not drop the term $\rho_p/\Delta\rho$, such that the process can be interpreted as a free fall under the *reduced gravity* due to buoyancy,

$$g' = \frac{\Delta\rho}{\rho_p} g \quad (3)$$

2.1.2. Viscous limiting regime

In the viscous regime, the Stokes's drag model can be obtained analytically [24],

$$F_d = 3\pi d_p \mu_f v \quad (4)$$

which expresses F_d as a linear function of v . Substituting Eq. (4) into Eq. (1), the viscous terminal velocity, v_{IV} , at which the reduced gravity of the particle is counterbalanced by the viscous drag force, and the viscous characteristic time, τ_V , can be obtained (see Appendix A) as

$$v_{IV} = \frac{\Delta\rho g d_p^2}{18\mu_f} \quad (5)$$

$$\tau_V = \frac{\rho_p d_p^2}{18\mu_f} \quad (6)$$

2.1.3. Inertial limiting regime

In the fluid inertial limit, the drag force (inertial fluid force) is a quadratic function of velocity,

$$F_d = \frac{1}{2}C_d\rho_f v^2 A = \frac{\pi}{8}d_p^2 C_d \rho_f v^2 \quad (7)$$

where C_d is drag coefficient and A is the cross-sectional area of the sphere, i.e., $A = \pi d_p^2/4$. Substituting Eq. (7) into Eq. (1) yields the inertial terminal velocity and characteristic time (see Appendix B), respectively,

$$v_{I1} = \sqrt{\frac{4gd_p\Delta\rho}{3C_d\rho_f}} \approx \sqrt{2gd_p\frac{\Delta\rho}{\rho_f}} \quad (8)$$

$$\tau_I = \frac{\rho_p}{\Delta\rho g} \sqrt{\frac{4gd_p\Delta\rho}{3C_d\rho_f}} \approx \sqrt{\frac{2d_p\rho_p^2}{\rho_f\Delta\rho g}} = \sqrt{\frac{2d_p\rho_p}{g'\rho_f}} \quad (9)$$

Note that the approximate equality above is achieved by assuming $C_d = 2/3$, which is reasonable because C_d is known to plateau at the inertial limit [25]; a similar treatment is done in [15].

2.1.4. Macroscopic time scales

Three elementary time scales are formulated so far for the three flow regimes; τ_F is the time required for a particle to fall a distance d_p from rest under gravity, while τ_V and τ_I are characteristic times for a sedimenting particle to reach terminal velocity under viscous and inertial fluid forces, respectively.

For an assembly of particles, macroscopic time scales may be defined by considering the initial column height h_i . For the free-fall regime, the

time scale over a fall distance of h_i is simply

$$t_F = \sqrt{\frac{2h_i}{g'}} \quad (10)$$

which has no dependence on d_p , consistent with the previous observations in granular avalanches [15].

For the viscous and inertial limiting regimes, we define the macroscopic time scales respectively as

$$t_V = h_i/v_{tV} = \frac{18\mu_f h_i}{\rho_p d_p^2} \quad (11)$$

$$t_I = h_i/v_{tI} = h_i/\sqrt{2gd_p \frac{\Delta\rho}{\rho_f}} \quad (12)$$

The macroscopic time scales presented above will be used for normalization in our later analysis for different flow regimes in Section 4.

2.2. Dimensionless numbers and phase diagram

The macroscopic flow behaviors are controlled by a set of dimensionless numbers, which may be defined as the ratios of different (elementary) time scales, thus signifying the relative dominance of one mechanism over another. Following the definition in [15,16], we have the Stokes number

$$St = \frac{\tau_V}{\tau_F} = \frac{\rho_p d_p^2}{18\mu_f} \sqrt{\frac{g'}{2d_p}} \quad (13)$$

which is the ratio of the time scales characterizing the viscous sedimentation and free fall, and the density ratio

$$r_\rho = \frac{\tau_I}{\tau_F} = \sqrt{\frac{\rho_p}{\rho_f}} \quad (14)$$

which is the ratio of the time scales characterizing the fluid-inertial sedimentation and free fall. Note that Eq. (14) contains only ρ_p and ρ_f with the assumption of $C_d = 2/3$.

The third dimensionless number is the Reynolds number,

$$Re = \frac{\tau_V}{\tau_I} = \frac{\rho_p d_p^2}{18\mu_f} \sqrt{\frac{g' \rho_f}{2d_p \rho_p}} = \frac{St}{r_\rho} \quad (15)$$

which represents the ratio between the characteristic time scales of viscous and fluid-inertial sedimentations. It can be interpreted as the ratio of the other two numbers.

Dimensionless numbers are essential for dynamic similarity when performing small-scale numerical and physical modeling. For instance, it might be relevant to scale down a large-scale landslide to a small-scale column collapse experiment by keeping St and r_ρ (thus Re) the same. Using Eq. (13) and assuming densities and gravity to be invariant across scales, we have the following scaling rule,

$$\frac{\mu_{f1}}{\mu_{f2}} = \left(\frac{d_{p1}}{d_{p2}}\right)^{\frac{3}{2}} \quad (16)$$

where the subscripts 1 and 2 denotes two arbitrary length scales.

The dimensionless numbers can also be used to define the boundaries between different flow regimes. As shown in Fig. 1, Courrech du Pont et al. [15] found in wet granular avalanches that the boundaries between the free-fall, viscous, and inertial regimes are $St = 10$, $r_\rho = 4$, and $Re = 2.5$. In a later study of immersed granular chute flows, Cassar et al. [16] defined the three regimes conceptually with $St = 1$, $r_\rho = 1$, and

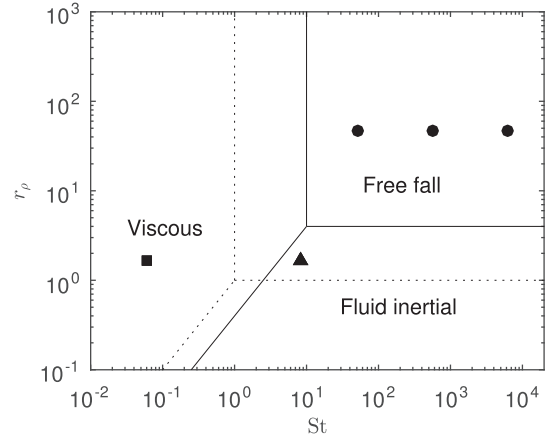


Fig. 1. Flow regimes defined in (St, r_ρ) space. The *solid* lines are boundaries experimentally identified by Courrech du Pont et al. [15], representing $St = 10$, $r_\rho = 4$, and $Re = 2.5$. The *dotted* lines are conceptual boundaries defined by Cassar et al. [16], representing $St = 1$, $r_\rho = 1$, and $Re = 1$. Markers refer to the test cases listed in Table 1: Circles: FL, FM, FS (from right to left); Triangles: IL, IM, IS (overlapped); Squares: VL, VM, VS (overlapped).

$Re = 1$. In our later analysis, we design the test cases in such a way that they are relevant to some realistic situations, and they fall into the three flow regimes defined in the literature (see our test plan in Section 3 and Fig. 1).

2.3. Scaling of particle contact properties

While the time scales discussed above are of major relevance to flow regimes in a coupled fluid-particle system, it is necessary to understand the scaling of particle contact properties that may alter the dynamics of a granular flow. We establish such a scaling by considering the collision of two identical particles. For simplicity, a linear spring-dashpot contact law [26,27] is assumed first and an extension to the Hertz model is discussed later. Let δ be the normal overlap of the two particles in collision, which have mass $m_p = \rho_p \pi d_p^3/6$, stiffness k and damping coefficient γ , we have the following equation of motion in terms of the overlap distance,

$$m_{\text{eff}} \ddot{\delta} = k\delta + \gamma \dot{\delta} \quad (17)$$

where $m_{\text{eff}} = m_p/2$ is the effective mass for two identical particles.

Considering material properties (m_p , k , γ) and gravity (g) to be basic quantities and applying length scale d_p and time scale $\sqrt{d_p/g}$, we obtain the scalings,

$$\tilde{\delta} = \frac{\delta}{d_p}, \tilde{\dot{\delta}} = \frac{\dot{\delta}}{\sqrt{gd_p}}, \tilde{\ddot{\delta}} = \frac{\ddot{\delta}}{g} \quad (18)$$

where the tilde symbol indicates normalized variables. The dimensionless equation of motion is then written as

$$\tilde{\ddot{\delta}} = \frac{2kd_p}{m_p g} \tilde{\delta} + \frac{2\gamma}{m_p} \sqrt{\frac{d_p}{g}} \tilde{\dot{\delta}} \quad (19)$$

We can define \tilde{k} and $\tilde{\gamma}$ as dimensionless stiffness and damping parameter, which have the forms

$$\tilde{k} = \frac{2kd_p}{m_p g} \propto \frac{k}{d_p^2}, \tilde{\gamma} = \frac{2\gamma}{m_p} \sqrt{\frac{d_p}{g}} \propto \frac{\gamma}{d_p^{5/2}} \quad (20)$$

which show that k and γ have to be scaled properly with d_p to achieve dynamic similarity. For the linear spring-dashpot contact model, the scaling rules for stiffness and viscous damping are

$$\frac{k_1}{k_2} = \left(\frac{d_{p1}}{d_{p2}}\right)^2, \frac{\gamma_1}{\gamma_2} = \left(\frac{d_{p1}}{d_{p2}}\right)^{\frac{5}{2}} \quad (21)$$

with the subscripts 1 and 2 denoting two arbitrary length scales.

The scaling of material properties can be extended to Hertz-type contact models, where k and γ are no longer constants. There exist different Hertz models in the literature, which differ mainly in the form of viscous damping [26,28,29]. Our simulations are performed with the formulation given in [30], which conveniently takes measurable material properties (e.g., Young's modulus E and the coefficient of restitution e) as input parameters. The details of this model is given in Appendix C.2, from which one can easily show that, for two identical particles, $k \propto E\sqrt{d_p\delta} \propto Ed_p$ and $\gamma \propto \beta\sqrt{E\sqrt{d_p\delta}d_p^3} \propto \beta\sqrt{Ed_p^2}$, where β is a dimensionless function of e ,

$$\beta = \frac{\ln e}{\sqrt{\ln^2 e + \pi^2}} \quad (22)$$

Combining with the scalings in Eq. (20) and Eq. (21), we have

$$\frac{E_1}{E_2} = \frac{d_{p1}}{d_{p2}}, e_1 = e_2 \quad (23)$$

where the subscripts 1 and 2 denotes two length scales, indicating that two such granular systems have the same dimensionless elastic and damping properties if the Young's modulus scales with length, while the coefficient of restitution remains constant. One can easily show that the tangential contact properties follow the same scalings (from Appendix C.2). Note that our scaling rules are obtained based on the specific Hertz model in Appendix C.2; different Hertz models may lead to different scalings especially for the viscous damping property (e.g., see [31]). Note also that since our results show a negligible role played by particle-scale dynamics, the details of the contact model is not crucial to the overall dynamics of the current coupled fluid-particle system.

3. Methodology

We adopt a numerical method that couples the discrete element method (DEM) and the computational fluid dynamics (CFD), known as CFD-DEM. It has the advantage of solving fluid-particle interactions at a low computational cost, allowing efficient three-dimensional simulations (see Appendix C for a detailed description). Recently, we have validated the CFD-DEM framework against multiple benchmark problems in [32] and further used it to simulate dry and underwater granular collapses in [9]. The model setup and test plan of this study are given as follows.

3.1. Model setup

Fig. 2(a) illustrates the setup of our numerical experiments. The initial packing is generated by pouring particles into the simulation box, cycling to equilibrium, and trimming the resultant column at a designated height. Each granular column consists of a slightly polydisperse packing of particles (i.e., a Gaussian distribution with mean diameter d_p and standard deviation $0.1d_p$). Note that d_p is a variable to be discussed later along with Table 1. Since the focus of the current study is the different flow regimes emerging with a variety of particle size, fluid viscosity, and fluid density, all columns have a consistent geometry. The initial length is $l_i = 30d_p$ and initial height is $h_i = 30d_p$, hence an aspect ratio of 1; the influence of varying aspect ratios has been investigated in [9]. The initial bulk packing density for all cases is around 0.56.

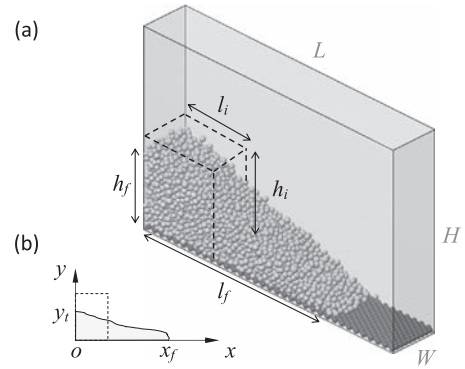


Fig. 2. Setup and notation. (a) The three-dimensional model in CFD-DEM (final state). The dashed lines indicate the initial column. The computational domain is filled with fluid. (b) Definition of front position x_f and top height y_t at an arbitrary time.

The computational domain is a rectangular box of length $L = 150d_p$, height $H = 80d_p$, and width $W = 10d_p$, filled with fluid. Periodic boundary conditions are imposed in the width direction in both CFD and DEM to represent a quasi-two-dimensional configuration, and we have verified that the domain size is sufficient to avoid boundary effects. The coordinate system of the quasi-two-dimensional problem is shown in Fig. 2(b), with the front position x_f and top height y_t marked for an arbitrary time t after the release of the initial mass. In CFD, non-slip boundary conditions are applied to all other walls, including the bottom of the box. In DEM, walls are frictional with the same coefficient of friction as particles, and the bottom is roughened by a layer of immobile base particles (diameter $d_b = d_p$) with a triangular close packing [33].

The fluid properties used in CFD, including density ρ_f and viscosity μ_f , are given in Table 1. In DEM, the following model parameters apply to both bulk and base particles: density $\rho_p = 2650 \text{ kg/m}^3$, Poisson's ratio $\nu = 0.24$, the coefficient of friction $\mu_p = 0.5$, and the coefficient of restitution $e = 0.5$. The Young's modulus E is a variable properly scaled according to Section 2.3 (see Table 1). Note that relatively low values of E ranging from $5 \times 10^7 \text{ Pa}$ to $1.25 \times 10^9 \text{ Pa}$ (while the laboratory value for glass beads is about $5 \times 10^{10} \text{ Pa}$) are deliberately chosen due to the computational cost especially for very fine particles ($d_p = 0.2 \text{ mm}$). Nevertheless, we have tested with $d_p = 1 \text{ mm}$ that such a reduction of E has a negligible influence for all ambient fluids used (see Appendix D).

The size of computational cells in CFD is $2d_p$; the numerical convergence towards this resolution has been verified. The time steps in DEM and CFD are 10^{-6} s and 10^{-5} s , respectively, such that coupling is made every 10 DEM cycles [32,34].

3.2. Test plan

In order to test the relevance of the derived dimensionless numbers St , r_p , and Re in different flow regimes, as well as the scaling rules given in Section 2, we design three sets of numerical tests corresponding to

Table 1

Test plan. For all cases, $\rho_p = 2650 \text{ kg/m}^3$, $\mu_p = 0.5$, $e = 0.5$, $\nu = 0.24$.

Regime	ID	d_p (mm)	E ($\times 10^7$ Pa)	μ_f (mPa·s)	ρ_f (kg/m ³)	St	r_p	Re
Free-fall	FL	5	125	0.18	1.2	6403	46.99	136.25
	FM	1	25	0.18	1.2	572.69	46.99	12.19
	FS	0.2	5	0.18	1.2	51.22	46.99	1.09
Inertial	IL	5	125	11.2	1000	8.12	1.63	4.99
	IM	1	25	1	1000	8.14	1.63	5.00
	IS	0.2	5	0.09	1000	8.13	1.63	5.00
Viscous	VL	5	125	1500	1000	0.06	1.63	0.037
	VM	1	25	134	1000	0.06	1.63	0.037
	VS	0.2	5	12	1000	0.06	1.63	0.037

the free-fall, inertial, and viscous regimes (see Table 1). In each regime, we have three sub-cases, involving respectively large-, medium-, and small-sized particles, with a controlled Stokes number (by adjusting fluid viscosity according to Eq. (16)) and density ratio. Young's modulus is scaled with particle size according to Eq. (23), while other particle properties (including density) remain constant. The case ID consists of two letters, indicating the specific combination of flow regime (F for free-fall, I for inertial, and V for viscous) and particle size (L for large, M for medium, and S for small). The calculated values of St , r_p , and Re listed in the table are also used to locate the nine cases in Fig. 1.

In the free-fall regime (or, dry cases), we use the properties of air to estimate St and r_p , although the simulations are performed only in DEM following the convention in the literature [13,35–38]. As we do not scale the properties of air with d_p , the value of St varies in the free-fall regime (Table 1); nevertheless, the specific value of St has no effect in this regime because only gravity is the dominant mechanism.

In the inertial and viscous regimes, where an actual ambient fluid is present, we fix the fluid density to $\rho_f = 1000 \text{ kg/m}^3$, but adapt viscosity according to Eq. (13) or Eq. (16) to control a constant combination of St and r_p . As listed in Table 1, the values of St are around 8.13 and 0.06 in the two limiting regimes, respectively. In the inertial regime, for instance, a column with larger particles ($d_p = 5 \text{ mm}$) has to be put in a more viscous fluid ($\mu_f = 11.2 \text{ mPa}\cdot\text{s}$), which is similar to the oil used in [6], such that it behaves similarly to the smaller particles ($d_p = 1 \text{ mm}$) immersed in water ($\mu_f = 1 \text{ mPa}\cdot\text{s}$). This theoretical prediction of dynamic similarity is to be tested in our simulations in the next section.

4. Results and discussions

In this section, we verify the dynamic similarity for each combination of Stokes number and density ratio. The phenomenological results are presented in Section 4.1 and Section 4.2, where we observe three different collapse dynamics in different flow regimes. Then, quantitative results are shown in Section 4.3 and Section 4.4. The results of a recent similar work [21] are discussed in Section 4.5.

4.1. Phenomenology

Fig. 3 presents a sequence of snapshots illustrating the flow characteristics of each flow regime, that is, free-fall (first row), inertial (second row), and viscous (third row). The cases with medium-sized particles ($d_p = 1 \text{ mm}$) are taken for example. For each case, we select four typical moments corresponding to the initial, fast-collapse (i.e., peak vertical kinetic energy), fast-spread (i.e., peak horizontal kinetic energy), and final states; the evolution of kinetic energy can be found in Section 4.4.

In general, the free-fall (FM) and inertial (IM) cases exhibit a similar process, where fracturing occurs from the top-right corner and a layer of mobilized particles slide down a self-formed slope. The location of the fracture surface, indicated by the color map of particle velocities, is similar in both cases; the approximate slope of the flowing layer is related to the frictional property of particles [39]. As the flow propagates down-slope, the flowing layer becomes shallower, forming a thin tip in the frontal region. Different features in the FM and IM cases may develop from this stage onwards. In case FM, high velocities are more concentrated near the front, and a small number of energetic particles become detached from the main flow (Fig. 3(c) and Fig. 3(d)). By contrast, the front in case IM is thicker, and no particle detachment is observed. The thicker front in case IM leads to a slightly concave surface morphology in the final deposit, which differs from the nearly triangular final shape in case FM. A vortex is generated in the background fluid of case IM (indicated by arrows), which propagates in the major flow direction of the particles. The horizontal propagation of the fluid eddy is a signature of the dominance of fluid inertia.

In the viscous case (VM), we observe a remarkably different phenomenon. Instead of the fracturing and sliding of a shear layer of particles, the particles near the top-right corner tend to fall towards the bottom. The falling particles are suspended by the ambient fluid, forming a region of relatively uniform velocities (see the distribution of the bright color in Fig. 3(j)), which is a viscous behavior due to the very small Stokes number ($St = 0.06$). Unlike the fast propagation of the leading edge of the initial column in the FM and IM cases, the toe of the initial column in the VM case remains nearly stagnant in the first few instants of time, and the vertical motion is more significant than the horizontal spreading. The process of this viscous collapse is more dynamically presented in Fig. 4 with flow-depth profiles selected

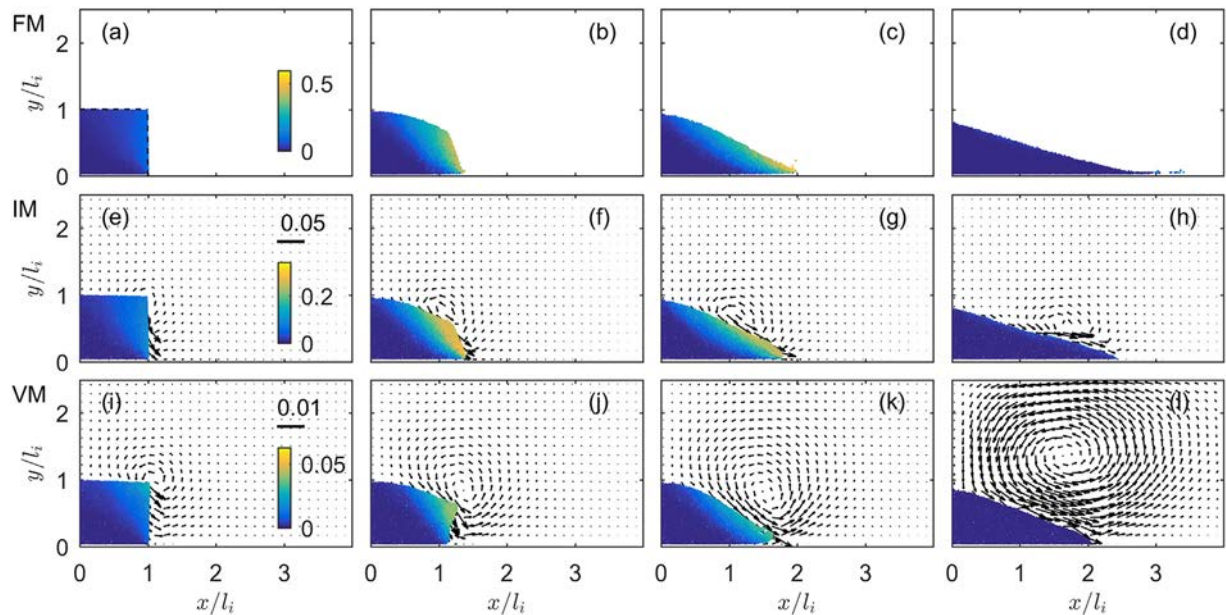


Fig. 3. Sequences of snapshots for the three medium-sized cases with $d_p = 1 \text{ mm}$, from top to bottom, representing the free-fall, inertial, and viscous regimes. (a–d) Case FM at four time instances $t/t_i = 0.2, 1, 1.8, 5$. (e–h) Case IM at $t/t_i = 0.1, 0.5, 0.8, 2$. (i–l) Case VM at $t/t_v = 0.02, 0.1, 0.18, 0.6$. Color bars indicate the magnitude of particle velocities with the unit of m/s. Arrows show the velocity vectors for a central slice of the fluid, with the scale bars shown in (e) and (i), respectively (unit: m/s).

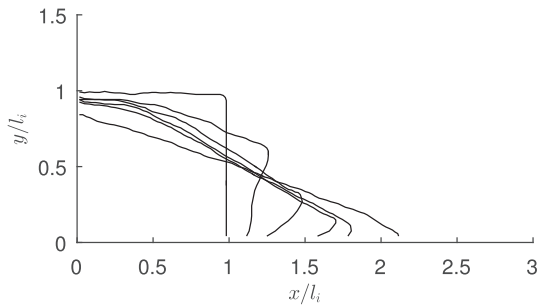


Fig. 4. Dynamic process of the viscous collapse (case VM). Lines are flow-depth profiles at $t/t_v = 0, 0.1, 0.15, 0.2, 0.25, 1$.

at several consecutive moments. The profiles are generated by evaluating local solid fractions in a set of virtual grids; solid fraction smaller than a threshold indicates the pure fluid phase. The duration of the viscous collapse is significantly longer (about 8 s) than the other two cases (within 1 s). In the meantime, a vortex is generated in the viscous fluid, which seems to recirculate slowly over a large area (Fig. 3(i)), instead of propagating in the horizontal direction (Fig. 3(h)). Note the scale bars in Figs. 3(e) and 3(i); the scale is 5 times larger in case IM than in case VM.

The different flow characteristics in the three regimes result in different deposit morphology. A comparison of the final deposits is presented in Fig. 5. While the FM and IM cases are only distinguishable in the frontal region (sharper in case FM), the VM case has a different deposit shape (shorter, thicker, and concave). By coloring particles according to their initial position (see the inset of Fig. 5(a)), the distinct features of final deposition can be associated with the different dominance of fracturing and falling behaviors. Note that we color the initial column as annular zones to highlight the different types of motion of the top-right corner. In the fracturing case (i.e., Fig. 5(a) and Fig. 5(b)), the particles in the final frontal region come from the entire leading edge of the initial column, hence a mixture of red and dark gray colors. The dark gray particles invade the bottom of red particles, showing the tendency of fracturing and sliding (the fracture surface is approximately within the dark gray region). By contrast, in the falling-dominant viscous collapse (i.e., Fig. 5(c)), the deposit front is occupied by particles originating from the corner. The boundary between the red and dark gray regions indicates how the particles from the corner settle and

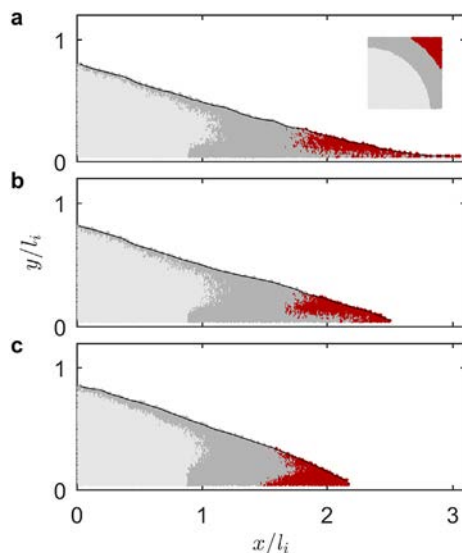


Fig. 5. Final deposit morphology of cases (a) FM, (b) IM, and (c) VM. Particles are colored according to their initial positions (Inset of (a)). Light gray: inner circle; Gray: middle ring; Red: corner. (For interpretation of the references to color in this figure legend, the reader is referred to the web version of this article.)

fold the particles from the lower part, leading to the concave deposit morphology.

4.2. Dynamic similarity

Next we test the dynamic similarity over different length scales with controlled Stokes number, density ratio, and scaled Young's modulus. In Fig. 6, the results of all nine test cases listed in Table 1 are presented. The time instances are the same as those in Fig. 3, but now we overlap the flow-depth profiles of the three sub-cases of large, medium, and small particles. Excellent agreement is observed in all three regimes. Note that the cases with the same St and r_ρ (and scaled Young's modulus) are not identical due to a randomized difference introduced in the generation of initial packings.² It is important to see that although we also scale Young's modulus with particle size, its influence is rather minor according to our discussion in Appendix D. Therefore, the agreement in Fig. 6 confirms that the dynamics of the present system is indeed controlled by the Stokes number and density ratio (but not particle properties).

4.3. Quantitative data: front position and flow thickness

Fig. 7 presents the quantitative data regarding front position and flow thickness, which are commonly used to characterize the dynamics of column collapses in the literature [10–12]. The raw data with physical units are presented in the inset graph of each subplot for reference, but our analyses below focus on the main graphs where dimensionless quantities are used. In particular, we made the travel distance $x_f - l_i$ and fall distance $y_f - h_i$ dimensionless by applying l_i and h_i as the length scales, respectively. Time t is normalized by the macroscopic time scales, t_F , t_v , and t_i , for the three regimes respectively, which are derived in Section 2.1.4. In each subplot, an error bar is used to show the maximum uncertainty of the numerical results, which is obtained by running five repeated simulations with varying random seeds during the generation of the initial packings (for $d_p = 1$ mm only). In general, the results across different scales collapse onto a single master curve in each subplot, showing again the dynamic similarity achieved by controlling the relevant dimensionless numbers.

The upper row of Fig. 7 presents the front propagation of the three regimes, i.e., free-fall, inertial, and viscous, respectively, from left to right. In Fig. 7(a), the three dry cases, FL, FM, FS, are shown as the solid, dashed, and dotted lines, respectively. A nearly constant-velocity stage can be observed (i.e. a constant slope between $t/t_F = 1$ and 3), which agrees with the previous findings in the literature [7,9–11]. The curves become non-smooth near the stoppage phase, owing to the detachment of particles as seen in Fig. 3(d). Note that we exclude these isolated particles when determining x_f . Although the three lines deviate slightly from each other in the final stage, the deviation is within the maximum error bar caused by the simulation uncertainty itself. In addition, the dimensionless duration for these flows to arrest is around 3.5, which is close to the value of 3.3 in the literature [10,11].

In the fluid-inertial cases (Fig. 7(b)), the dimensionless front position evolves similarly compared to the dry cases in Fig. 7(a). A major difference is that it approaches the final stage more smoothly and the uncertainty (error bar) is smaller, since the discrete behaviors of particles in the front region is largely suppressed in the immersed cases (see Fig. 3(g)). The dimensionless duration of inertial collapses is about $t/t_i = 2.5$.

In the viscous cases (Fig. 7(c)), the propagation of front position has a different feature. Two main stages can be observed, with a steep acceleration stage and a slowly-evolving final stage. The first stage corresponds to the falling process noted in Fig. 3(j), while the second stage

² Particles are inserted to the computational domain at a controlled insertion rate, which is not scaled in our practice. Nevertheless, the influence caused by a randomized initial packing is minor; see error bars in Fig. 7.

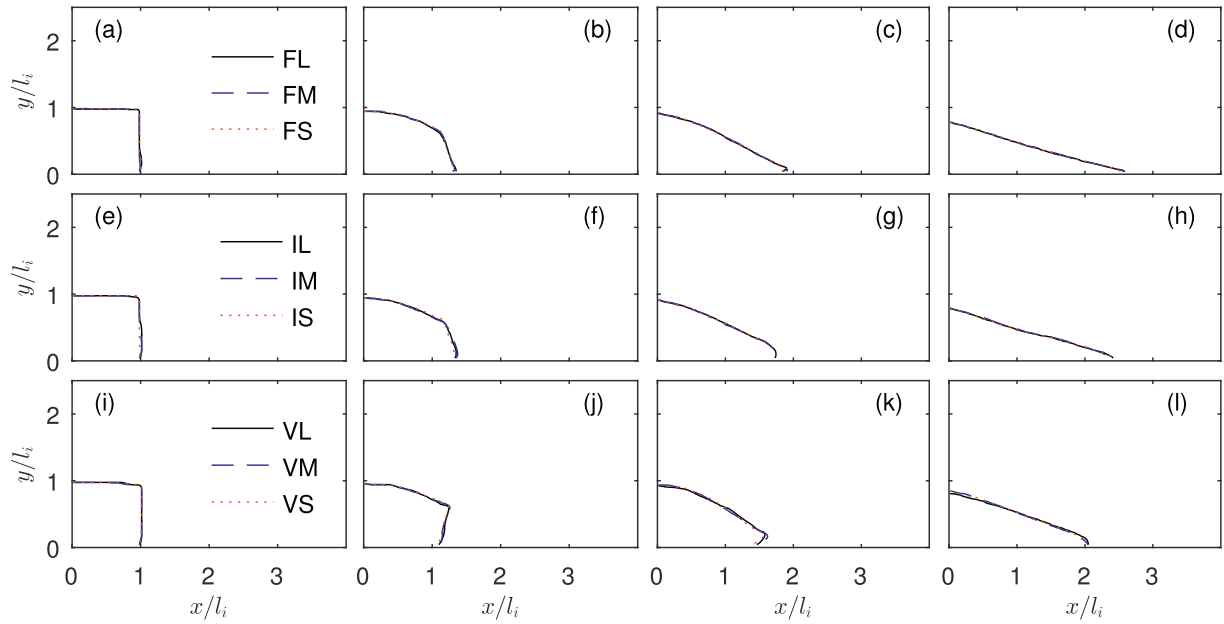


Fig. 6. Flow-depth profiles showing the dynamic similarity of the three sub-cases of large, medium and small particles in each regime. (a–d) Free-fall regime; four dimensionless time instances $t/t_F = 0.2, 1, 1.8, 5$. (e–h) Inertial regime; $t/t_I = 0.1, 0.5, 0.8, 2$. (i–l) Viscous regime; $t/t_V = 0.02, 0.1, 0.18, 0.6$.

reflects the fact that the viscous collapse come to a final halt very slowly (i.e., creeping regime). Note that in the viscous regime, the definition of the “front” may be ambiguous, because the leading point of the flow is no longer the point propagating at the bottom, but rather the furthest corner suspended in the fluid (see e.g. Fig. 3(j)). Here we still define x_f as the point at which the flow-depth profile touches the bottom; we have verified that using the furthest point as an alternative definition of x_f only introduces a systematic change for early stages but does not affect our discussion.

In the second row of Fig. 7, the fall distance of the top surface, $y_t - h_i$, which is normalized by h_i , is plotted as a function of dimensionless

time. It is notable that the curves (especially for larger scales) are largely stepwise, which is attributed to the slow decrease of flow thickness (in the vicinity of $x = 0$) close to an inherent microscopic length scale set by the particle size ($d_p/h_i = 0.033$ in all cases); indeed, the height of each step is roughly around the particle size (e.g., about 0.03 for case FL in Fig. 7(d)). The size of the error bars in Figs. 7(d–f) is larger for the same reason. All three curves in each regime tend to converge after normalization, with discrepancies smaller than the measurement errors. The drop of height in Fig. 7(f) is significantly less than those in Figs. 7(d) and (e), indicating a clearly thicker deposit in the viscous cases.

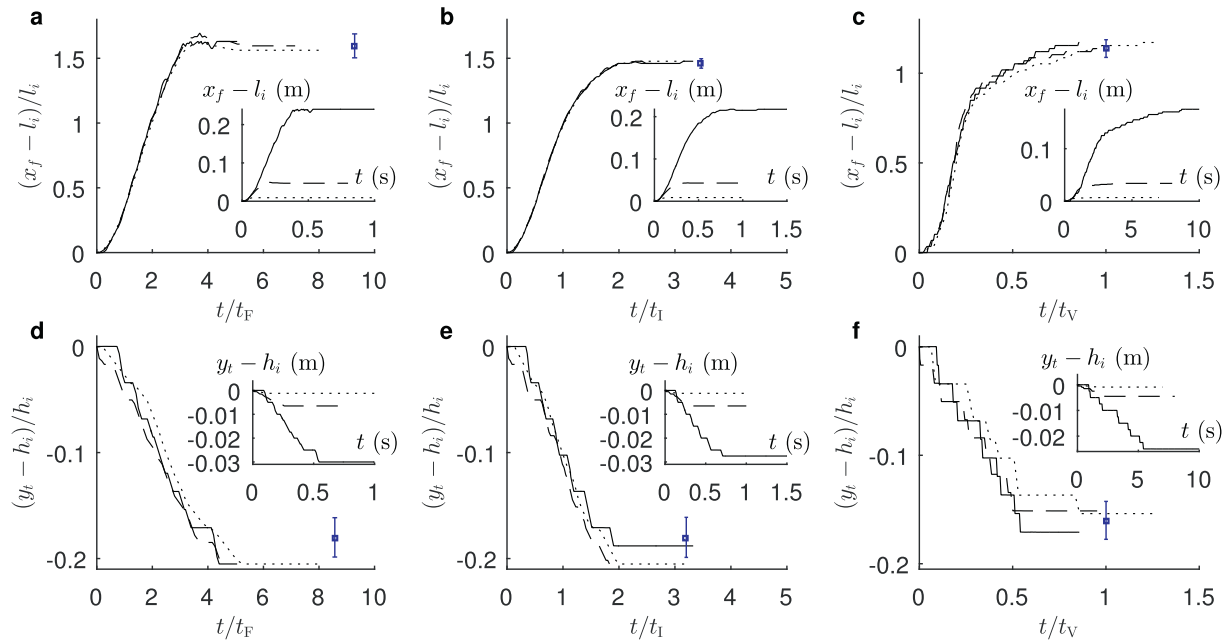


Fig. 7. Temporal evolutions of front position (x_f) and top height (y_t), from left to right, representing the free-fall, inertial, and viscous regimes, respectively. In all subgraphs, the solid, dashed and dotted lines refer to the cases of large, medium, and small particles, respectively. The error bars show the maximum standard deviations caused by varying random seeds (in $d_p = 1$ mm cases), which are only visible at the deposition stage. (a–c) The normalized travel distance $(x_f - l_i)/l_i$ as a function of the normalized time. Insets: $x_f - l_i$ as a function of t with physical units. (d–f) The normalized fall distance $(y_t - h_i)/h_i$ as a function of the normalized time. Insets: $y_t - h_i$ as a function of t with physical units.

4.4. Quantitative data: kinetic energy

The temporal evolution of kinetic energy is commonly used to understand the dynamics of granular collapses [8,9,13,35,37,39,40]. Here we consider the “partial” kinetic energy in x and y directions for both the fluid and particulate phases. Partial kinetic energies are calculated from the horizontal and vertical velocity components [8,13,37]. For particles, we have

$$E_{kx}^p = \frac{1}{2} \sum_{i=1}^{n_p} m_i u_i^2 \quad (24a)$$

$$E_{ky}^p = \frac{1}{2} \sum_{i=1}^{n_p} m_i v_i^2 \quad (24b)$$

where m_i is the mass of particle i , u_i and v_i are velocities of particle i in x and y directions, respectively, and n_p is the total number of particles. For fluid, we have

$$E_{kx}^f = \frac{1}{2} V_{fc} \sum_{i=1}^{n_{fc}} \alpha_f \rho_f u_f^2 \quad (25a)$$

$$E_{ky}^f = \frac{1}{2} V_{fc} \sum_{i=1}^{n_{fc}} \alpha_f \rho_f v_f^2 \quad (25b)$$

where u_f and v_f are local fluid velocities in x and y directions, respectively, α_f is porosity, V_{fc} is the volume of a fluid cell, and n_{fc} is the total number of fluid cells.

Since the collapse of a column is driven by the drop of potential energy of particles, the initial potential energy E_0 is used to normalize the kinetic energy, which is defined as

$$E_0 = \sum_{i=1}^{n_p} m_i g h_{ci} \quad (26)$$

where h_{ci} is the initial height of the centroid of particle i .

Fig. 8(a) shows the normalized partial kinetic energy (of particles) for the free-fall regime, with black and gray colors representing the x and y directions respectively, and different line types indicating different particle sizes. After normalization, the energy evolution collapses for different particle sizes; small discrepancies exist near the peaks, which might stem from the randomized difference in the generation of initial packings, as discussed with Figs. 6 and 7. Apart from this small difference, it is observed that both E_{kx}^p and E_{ky}^p increase simultaneously from the beginning, with the latter evolving slightly faster but the former towards a higher peak. This behavior corresponds to the shear flow along the self-formed slope discussed in Fig. 3(a), showing that the horizontal spreading is dominant over the vertical movement. Both E_{kx}^p and E_{ky}^p are entirely dissipated after $t/t_F = 5$.

Fig. 8(b) shows the energy evolution of the three fluid-inertial cases. Particle kinetic energies are presented in the main axes, which exhibit a similar trend with the curves in Fig. 8(a). The absolute values of peak E_{kx}^p and E_{ky}^p are roughly half of those in Fig. 8(a), owing to the energy transmission via fluid-particle interactions and the viscous dissipation in the fluid. In the inset of Fig. 8(b), the partial fluid kinetic energies are presented. It can be observed that the particle size has nearly no influence on the normalized fluid energy. The peak of E_{kx}^f is higher than that of E_{ky}^f , consistent with the more profound horizontal motion of the fluid. It takes much longer time for the energy to dissipate in the fluid than in the particles.

For the three viscous cases (Fig. 8(c)), two major differences can be observed. Firstly, the particle kinetic energy in the vertical direction, E_{ky}^p , reaches a higher peak than E_{kx}^p , in contrast to the case in the free-fall and inertial regimes. This is a distinct feature of the viscous collapses, where

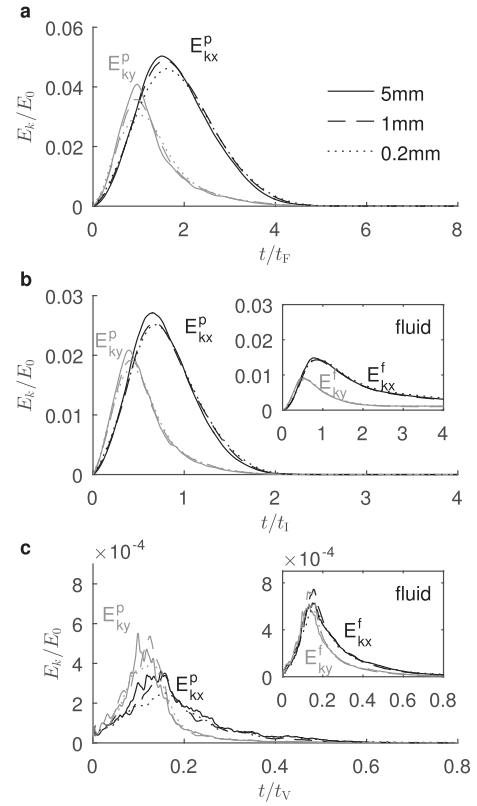


Fig. 8. Evolutions of normalized kinetic energy (E_k/E_0) in the vertical and horizontal directions. (a) Free-fall regime. (b) Inertial regime. Inset: Kinetic energy of fluid. (c) Viscous regime. Inset: Kinetic energy of fluid.

the vertical fall is more dominant than the horizontal spread (see Fig. 4). Secondly, the magnitudes of E_{kx}^p and E_{ky}^p are significantly small in the viscous regime (creeping motions), while the fluid energies, E_{kx}^f and E_{ky}^f , are slightly higher than E_{kx}^p and E_{ky}^p . The latter is attributed to the fact that a large volume of fluid is mobilized, which remains in a slow recirculation (see the arrows in Figs. 3(k-l)). The fluid energies are well scaled for the three particle sizes.

4.5. Discussion on a recent work

During the preparation of this paper, an experimental study has been published regarding the flow regimes in immersed granular collapses [21]. Similar to the way we establish the phase diagram in Fig. 1 (b), Bouguin et al. [21] followed the same idea in [15] to formulate Stokes number and density ratio based on a single-particle scenario and test the relevance of these numbers in immersed granular collapses. From the snapshots reported in [21], it is interesting to see similar results in the dry and fluid-inertial regimes when the aspect ratio is 1, and also the largely suppressed horizontal spreading in the viscous regime (especially when the aspect ratio is high).

While we use a coupled fluid-particle method in this research, Bouguin et al. [21] performed laboratory experiments and focused on densely-packed columns (the packing density is around 0.64, much higher than our average value of 0.56), which are known to exhibit a delay of collapse [6]. The results in [21] suggest that except packing density, the Stokes number also controls the triggering time, which tends to increase when St decreases. In fact, a similar delay of spreading is also observed in our viscous cases (see Fig. 8(c)) in spite of the relatively loose initial packing. Another focus of [21] is the effect of aspect ratio. It is well known in granular collapse problems that runout distance is a piecewise power-law function of the initial aspect ratio [6,10], and Bouguin et al. [21] showed such scaling

functions for a variety of St. Our recent work [9] also studied the runout scaling of underwater granular collapse in detail, where we relied on energy arguments (as we have access to particle and fluid velocities in our simulations) to explain the piecewise power-law scaling functions. Bougouin et al. [21] further provided a modified phase diagram for Fig. 1, where the initial column height is incorporated. It is an interesting future direction to compare our results with the data reported in [21], and utilize the numerical method to study local variables (e.g., packing density, velocity, shear rate, stress tensor) that are relevant to granular and suspension rheology [17,18].

5. Concluding remarks

In this paper, we study the flow regimes and dynamic similarity during the collapse of immersed granular columns. We first derive different dimensionless numbers (Stokes number St and density ratio r_ρ) based on typical time scales related to the motion of a sedimenting sphere, and then test the relevance of these dimensionless numbers with coupled continuum-discrete simulations. With St ranging from 0.06 to 6403 and r_ρ from 1.63 to 46.99, our results show three regimes with different flow dynamics, i.e., free-fall, fluid-inertial, and viscous regimes, which can be well determined by a phase diagram combining St and r_ρ . The collapse dynamics exhibit a transition from sliding-dominant to suspension-dominant behaviors as St decreases towards a small value. In each regime, we achieve dynamic similarity regarding front position and flow thickness for three different particle sizes, by properly scaling fluid viscosity according to the Stokes number. The dynamic similarity confirms that St is the major controlling dimensionless parameter for immersed granular collapses, while particle-scale dynamics play a minor role in the overall flow behaviors. The understanding represents a major contribution of this work.

Furthermore, the role of Young's modulus is discussed. It is found that despite the exaggerated discrepancy of peak kinetic energies, flow-depth profiles (including the final deposit morphology) are insensitive to the choice of Young's modulus. Therefore, it is proper to use a relatively low Young's modulus to improve computational efficiency, such that simulations of larger samples and finer particles are affordable in coupled discrete-continuum simulations.

The understanding of the flow regimes and scaling rules is crucial in industrial and geological applications involving immersed granular flows. In particular, we derived the following scaling rules for fluid viscosity and particle properties (for the specific contact model we use): $\mu_{f1}/\mu_{f2} = (d_{p1}/d_{p2})^{3/2}$, $E_1/E_2 = d_{p1}/d_{p2}$, and $e_1/e_2 = 1$, with other properties (e.g., fluid density, particle density, and the coefficient of friction) remaining constant. The scaling rules are useful for down-scaled experiments, for instance, where large particles may be combined with a more viscous fluid such that a certain industry-scale situation can be reproduced. Furthermore, the numerical method used in this study permits access to internal flow properties, which are of potential interest to future work regarding dry and wet granular rheology and thus large-scale continuum modeling of granular flows.

Acknowledgements

The work was supported by Research Grants Council of Hong Kong (Grant No. 17203614) and FAP-DF, Brazil. This research was conducted in part using the research computing facilities and advisory services offered by Information Technology Services, The University of Hong Kong.

Appendix A. Solution of the equation of motion in viscous regime

The equation of motion for a sphere sedimenting in the viscous regime is given by

$$\frac{\pi}{6} d_p^3 \rho_p \frac{dv}{dt} = \frac{\pi}{6} d_p^3 \Delta \rho g - 3\pi d_p \mu_f v \quad (\text{A.1})$$

which can be rewritten into a first-order linear differential equation

$$\frac{dv}{dt} + \frac{18\mu_f}{\rho_p d_p^2} v = \frac{\Delta \rho}{\rho_p} g \quad (\text{A.2})$$

Applying the integrating factor method, we have the following general solution,

$$v = \frac{\Delta \rho g d_p^2}{18\mu_f} + C \cdot e^{-\frac{18\mu_f}{\rho_p d_p^2} t} \quad (\text{A.3})$$

where C is an arbitrary constant. Since the sedimentation starts from rest, i.e., $v = 0$ if $t = 0$, we have $C = -\Delta \rho g d_p^2 / 18\mu_f$.

Defining the *viscous characteristic time* and *viscous terminal velocity* as

$$\tau_v = \frac{\rho_p d_p^2}{18\mu_f} \quad \text{and} \quad v_{tV} = \frac{\Delta \rho g d_p^2}{18\mu_f}, \quad (\text{A.4})$$

respectively, we can write

$$v = v_{tV} (1 - e^{-t/\tau_v}) \quad (\text{A.5})$$

indicating that as $t \rightarrow \infty$, $v \rightarrow v_{tV}$. When $t = \tau_v$, we have $v = (1 - e^{-1})v_{tV} \approx 0.63v_{tV}$, which indicates that τ_v is the characteristic time for the sphere to obtain 63% of the viscous terminal velocity.

Appendix B. Solution of the equation of motion in fluid-inertial regime

The equation of motion for a sphere sedimenting in the inertial regime is

$$\frac{\pi}{6} d_p^3 \rho_p \frac{dv}{dt} = \frac{\pi}{6} d_p^3 \Delta \rho g - \frac{\pi}{8} d_p^2 C_d \rho_f v^2 \quad (\text{B.1})$$

which is rewritten as

$$\frac{dv}{dt} + \frac{3C_d \rho_f}{4d_p \rho_p} v^2 = \frac{\Delta \rho}{\rho_p} g \quad (\text{B.2})$$

Using the separation of variable method, we obtain

$$v = \sqrt{\frac{4gd_p \Delta \rho}{3C_d \rho_f}} \cdot \tanh \left(\frac{t}{\frac{\rho_p}{\Delta \rho g} \sqrt{\frac{4gd_p \Delta \rho}{3C_d \rho_f}}} \right) \quad (\text{B.3})$$

which satisfies the condition that $v = 0$ if $t = 0$.

Let τ_i and v_{ti} be the *inertial characteristic time* and *inertial terminal velocity*, respectively, as

$$\tau_i = \frac{\rho_p}{\Delta \rho g} \sqrt{\frac{4gd_p \Delta \rho}{3C_d \rho_f}} \quad \text{and} \quad v_{ti} = \sqrt{\frac{4gd_p \Delta \rho}{3C_d \rho_f}}, \quad (\text{B.4})$$

we simplify the solution to

$$v = v_{ti} \cdot \tanh(t/\tau_i) \quad (\text{B.5})$$

indicating that when $t \rightarrow \infty$, $v \rightarrow v_{ti}$. When $t = \tau_i$, we have $v = \tanh(1)v_{ti} \approx 0.76v_{ti}$, which indicates that τ_i is the characteristic time for the sphere to obtain 76% of the inertial terminal velocity.

Appendix C. Details of CFD-DEM

Appendix C.1. Governing equations

The CFD-DEM coupling is implemented with a combination of open source C++ libraries, namely, OpenFOAM and CFDEMproject. The former is a CFD toolbox [41], while the latter includes LIGGGHTS for DEM simulations and CFDEMcoupling for the data exchange between CFD and DEM [34].

In CFD, we solve the local-averaged Navier-Stokes equations [34,42,43],

$$\frac{\partial}{\partial t} (\alpha_f \rho_f \mathbf{u}_f) + \nabla \cdot (\alpha_f \rho_f \mathbf{u}_f \mathbf{u}_f) = -\alpha_f \nabla p + \alpha_f \nabla \cdot \mathbf{T}_f + \alpha_f \rho_f \mathbf{g} - \mathbf{f}_{pf} \quad (\text{C.1a})$$

$$\frac{\partial \alpha_f}{\partial t} + \nabla \cdot (\alpha_f \mathbf{u}_f) = 0 \quad (\text{C.1b})$$

where α_f is the volume fraction of fluid in each computational cell (i.e., porosity), $\mathbf{u}_f = (u_f, v_f, w_f)$ is the velocity vector of fluid, ρ_f is fluid density, p is pressure, $\mathbf{T}_f = \mu_f (\nabla \mathbf{u}_f + \nabla \mathbf{u}_f^T)$ is the extra-stress tensor of a fluid with viscosity μ_f , \mathbf{f}_{pf} is the interaction force acting from the fluid phase to the particulate phase (see Appendix C.3), and \mathbf{g} is the gravitational acceleration vector.

In DEM, the motion of particles is governed by the Newton's second law [34],

$$m_i \frac{d\mathbf{u}_i}{dt} = \sum_{j=1}^{n_i^c} \mathbf{F}_{ij}^c + \mathbf{F}_i^f + m_i \mathbf{g} \quad (\text{C.2a})$$

$$I_i \frac{d\boldsymbol{\omega}_i}{dt} = \sum_{j=1}^{n_i^c} \mathbf{M}_{ij}^c \quad (\text{C.2b})$$

where $\mathbf{u}_i = (u_i, v_i, w_i)$ denotes the translational velocity of particle i , \mathbf{F}_{ij}^c is the contact force on particle i by particle j or boundaries, \mathbf{F}_i^f is the particle–fluid interaction force acting on particle i , $\boldsymbol{\omega}_i$ is the particle angular velocity, I_i is the moment of inertia, and \mathbf{M}_{ij}^c is the moment acting on particle i by particle j or boundaries. The contact force \mathbf{F}_{ij}^c is calculated using a Hertz-type model (see Appendix C.2). The fluid force \mathbf{F}_i^f includes buoyancy force $\mathbf{F}_i^b = V_i (-\nabla p + \nabla \cdot \mathbf{T}_f)$, where V_i is the volume of particle i , and drag force \mathbf{F}_i^d (see Appendix C.3).

Appendix C.2. Contact model

The key ingredients of the Hertz contact model are presented to aid the understanding of the scaling of particle dynamics. The current Hertz model is detailed in [30]; different Hertz-type models exist in the literature [26,28,29], which mainly differ in the damping part. The current model has the advantage of using measurable material properties (i.e., Young's modulus E , Poisson's ratio ν , the coefficient of friction μ_p , and the coefficient of restitution e) as input parameters.

The contact force between particles i and j has the normal and tangential components, i.e.,

$$\mathbf{F}_{ij}^c = \mathbf{F}_{ij}^n + \mathbf{F}_{ij}^t \quad (\text{C.3})$$

which can be evaluated by summing the elastic and damping parts,

$$\mathbf{F}_{ij}^n = k_n \delta_n + \gamma_n \mathbf{v}_{ij}^n \quad (\text{C.4a})$$

$$\mathbf{F}_{ij}^t = k_t \delta_t + \gamma_t \mathbf{v}_{ij}^t \quad (\text{C.4b})$$

$$|\mathbf{F}_{ij}^t| \leq \mu_p |\mathbf{F}_{ij}^n| \quad (\text{C.4c})$$

where subscripts (or superscripts) n and t denote normal and tangential components, respectively, k and γ are elastic and damping parameters, δ is overlap vector (with δ_n being overlap distance), and \mathbf{v}_{ij} is the relative velocity at contact. The elastic and damping parameters are given as follows.

$$k_n = \frac{4}{3} E_{\text{eff}} \sqrt{R_{\text{eff}} \delta_n} \quad (\text{C.5a})$$

$$\gamma_n = 2 \sqrt{\frac{5}{6}} \beta \sqrt{S_n m_{\text{eff}}} \quad (\text{C.5b})$$

$$k_t = 8 G_{\text{eff}} \sqrt{R_{\text{eff}} \delta_n} \quad (\text{C.5c})$$

$$\gamma_t = 2 \sqrt{\frac{5}{6}} \beta \sqrt{S_t m_{\text{eff}}} \quad (\text{C.5d})$$

where S_n , S_t and β are parameters,

$$S_n = 2 E_{\text{eff}} \sqrt{R_{\text{eff}} \delta_n} \quad (\text{C.6a})$$

$$S_t = 8 G_{\text{eff}} \sqrt{R_{\text{eff}} \delta_n} \quad (\text{C.6b})$$

$$\beta = \frac{\ln e}{\sqrt{\ln^2 e + \pi^2}} \quad (\text{C.6c})$$

with E_{eff} , G_{eff} , R_{eff} , and m_{eff} being effective Young's modulus, shear modulus, radius, and mass, respectively, given by

$$\frac{1}{E_{\text{eff}}} = \frac{1-\nu_i^2}{E_i} + \frac{1-\nu_j^2}{E_j} \quad (\text{C.7a})$$

$$\frac{1}{G_{\text{eff}}} = \frac{2(2-\nu_i)(1+\nu_i)}{E_i} + \frac{2(2-\nu_j)(1+\nu_j)}{E_j} \quad (\text{C.7b})$$

$$R_{\text{eff}} = \frac{R_i R_j}{R_i + R_j} \quad (\text{C.7c})$$

$$m_{\text{eff}} = \frac{m_i m_j}{m_i + m_j} \quad (\text{C.7d})$$

where subscripts i and j indicate particles i and j respectively.

Appendix C.3. Fluid-particle interaction

The fluid-particle interaction is considered as a momentum exchange term in CFD,

$$\mathbf{f}_{pf} = K_{pf} (\mathbf{u}_f - \langle \mathbf{u}_p \rangle) \quad (\text{C.8})$$

where $\langle \mathbf{u}_p \rangle$ is the cell-based average particle velocity and K_{pf} is given by

$$K_{pf} = \frac{\sum_i F_i^d}{V_{fc} |\mathbf{u}_f - \langle \mathbf{u}_p \rangle|} \quad (\text{C.9})$$

where V_{fc} is the volume of computational cell, and F_i^d is the magnitude of drag force acting on individual particles in DEM, such that $\mathbf{F}_i^d = F_i^d (\mathbf{u}_f - \langle \mathbf{u}_p \rangle) / |\mathbf{u}_f - \langle \mathbf{u}_p \rangle|$.

We calculate the drag force using the Di Felice model [25],

$$F_i^d = \frac{1}{8} C_d \rho_f \pi d_i^2 |\mathbf{u}_f - \mathbf{u}_i| \alpha_f^{1-\chi} \quad (\text{C.10})$$

where d_i is the diameter of particle i , C_d is drag coefficient, and χ is a corrective coefficient. Both C_d and χ are a function of the particulate Reynolds number Re_p ,

$$C_d = \left(0.63 + \frac{4.8}{\sqrt{Re_p}} \right)^2 \quad (C.11a)$$

$$\chi = 3.7 - 0.65 \exp \left[-\frac{(1.5 - \log_{10} Re_p)^2}{2} \right] \quad (C.11b)$$

with

$$Re_p = \frac{\alpha_f \rho_f d_i |\mathbf{u}_f - \mathbf{u}_i|}{\mu_f} \quad (C.12)$$

which considers the local porosity, α_f , of a particulate system. Note that a different drag law [23,34] may be adopted in the CFD-DEM simulation, which may slightly affect fluid-particle interactions when Re_p is in a moderate range. The choice of the drag law is expected to not affect the conclusions drawn in this paper.

Appendix D. Effect of Young's modulus

As presented in Section 3.1 and Table 1, we adopt relatively low values of Young's modulus in order to accelerate our simulations, especially when fine particles ($d_p = 0.2$ mm) are used. To demonstrate that the reduction of Young's modulus only has a negligible impact on the runout and deposition of column collapses, we perform a sensitivity analysis on the values of Young's modulus by varying E from 2.5×10^8 Pa to 5×10^{10} Pa for the three medium-sized cases ($d_p = 1$ mm), i.e., FM, IM, and VM. The final deposits in the three regimes are

compared in Figs. 9(a–c), respectively, while the normalized energy evolutions are presented in Figs. 9(d–f).

One important conclusion made from Figs. 9(a–c) is that the variation of E over two orders of magnitude produces nearly identical final deposit morphologies, respectively, in the three flow regimes. In addition, similar to the comparison in Fig. 6, we have verified that the flow-depth profiles match well at a series of time instances (plots not shown for brevity). The convergence of flow-depth profiles (including front position) and final deposit shapes (including runout distance) demonstrates that the effect of particle stiffness is rather negligible in the current dynamic configurations. It is therefore reasonable to adopt a small value of E to improve the computational efficiency, which is potentially important for future studies involving larger columns and finer particles.

On the other hand, from the energy plots in Figs. 9(d–f) we observe discrepancies of normalized peak energies. For instance, the peak of E_{kx}^p tends to decrease as E increases. In other words, energy dissipation seems to be imperfectly scaled when particle stiffness varies. Considering the dimensionless stiffness and damping parameter established in Section 2.3, the dimensionless stiffness and damping parameter tend to increase when E increases or d_p decreases, which explains the tendency observed in Fig. 9(d–f) that the flow tends to gain a lower kinetic energy when Young's modulus increases. Note that total energy exaggerates the actual difference in local velocities, which is so small that the final deposit is not affected. The tendency that a higher stiffness leads to a lower kinetic energy has been reported previously in steady dense granular flows in both dynamic [29,44] and quasi-static [45] regimes. Nevertheless, the influence of dimensionless particle properties is considered to be negligible, since we identify the Stokes number and density ratio as the major dimensionless numbers that determine flow regimes and dynamics similarity combined with the major results in Fig. 3–Fig. 7.

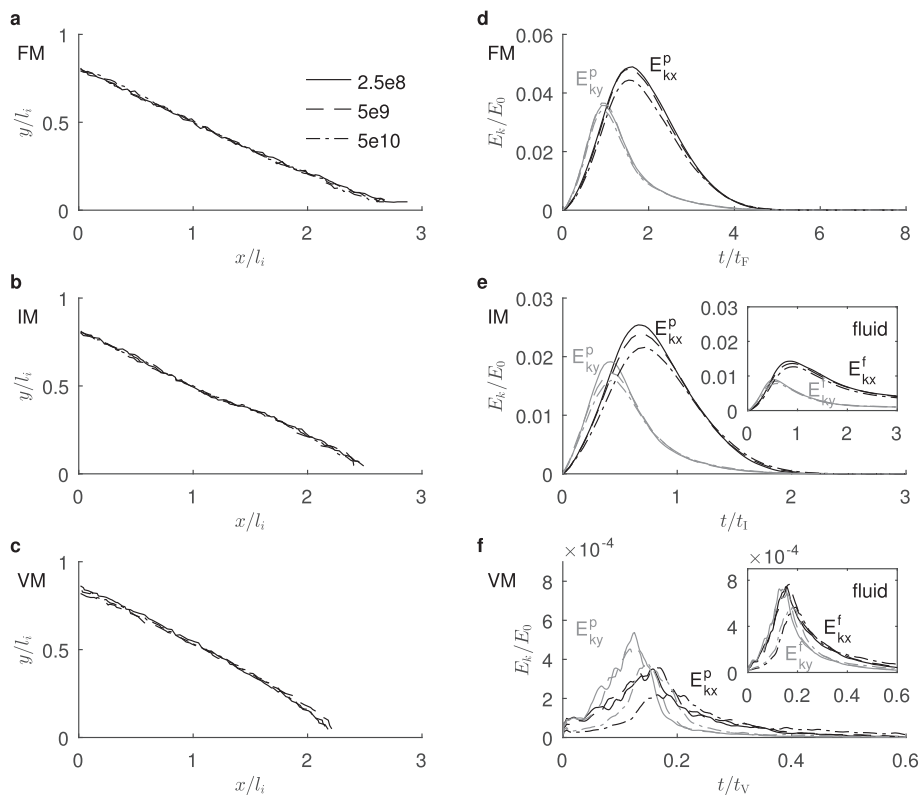


Fig. 9. Effect of Young's modulus in free-fall (upper row), inertial (middle row), and viscous (lower row) regimes. (For interpretation of the references to color in this figure legend, the reader is referred to the web version of this article.)

References

- [1] N. Jain, J.M. Ottino, R.M. Lueptow, Effect of interstitial fluid on a granular flowing layer, *J. Fluid Mech.* 508 (2004) 23–44, <https://doi.org/10.1017/S0022112004008869>.
- [2] F. Pignatelli, C. Asselin, L. Krieger, I. C. Christov, J. M. Ottino, R. M. Lueptow, Parameters and scalings for dry and immersed granular flowing layers in rotating tumblers, *Phys. Rev. E* 86 (1), <https://doi.org/10.1103/PhysRevE.86.011304>.
- [3] P. Frey, M. Church, How river beds move, *Science* 325 (5947) (2009) 1509–1510, <https://doi.org/10.1126/science.1178516>.
- [4] F. Lvholt, S. Bondevik, J.S. Laberg, J. Kim, N. Boylan, Some giant submarine landslides do not produce large tsunamis: giant landslide tsunamis, *Geophys. Res. Lett.* 44 (16) (2017) 8463–8472, <https://doi.org/10.1002/2017GL074062>.
- [5] E.L. Thompson, H.E. Huppert, Granular column collapses: further experimental results, *J. Fluid Mech.* 575 (2007) 177, <https://doi.org/10.1017/S0022112006004563>.
- [6] L. Rondon, O. Pouliquen, P. Aussillous, Granular collapse in a fluid: role of the initial volume fraction, *Phys. Fluids* 23 (7) (2011) 073301, <https://doi.org/10.1063/1.3594200>.
- [7] C. Meruane, A. Tamburrino, O. Roche, On the role of the ambient fluid on gravitational granular flow dynamics, *J. Fluid Mech.* 648 (2010) 381, <https://doi.org/10.1017/S0022112009993181>.
- [8] V. Topin, Y. Monerie, F. Perales, F. Radja, Collapse dynamics and runout of dense granular materials in a fluid, *Phys. Rev. Lett.* 109 (18), 188001, <https://doi.org/10.1103/PhysRevLett.109.188001>.
- [9] L. Jing, G.C. Yang, C.Y. Kwok, Y.D. Sobral, Dynamics and scaling laws of underwater granular collapse with varying aspect ratios, *Phys. Rev. E* 98 (4) (2018), 042901, <https://doi.org/10.1103/PhysRevE.98.042901>.
- [10] E. Lajeunesse, J.B. Monnier, G.M. Homsy, Granular slumping on a horizontal surface, *Phys. Fluids* 17 (10) (2005) 103302, <https://doi.org/10.1063/1.2087687>.
- [11] G. Lube, H. E. Huppert, R. S. J. Sparks, A. Freundt, Collapses of two-dimensional granular columns, *Phys. Rev. E* 72 (4), 041301, <https://doi.org/10.1103/PhysRevE.72.041301>.
- [12] N.J. Balmforth, R.R. Kerswell, Granular collapse in two dimensions, *J. Fluid Mech.* 538 (2005) 399, <https://doi.org/10.1017/S0022112005005537>.
- [13] L. Staron, E.J. Hinch, Study of the collapse of granular columns using two-dimensional discrete-grain simulation, *J. Fluid Mech.* 545 (2005) 1, <https://doi.org/10.1017/S0022112005006415>.
- [14] T. Zhao, Investigation of Landslide-Induced Debris Flows by the DEM and CFD, Ph.D. thesis, University of Oxford, 2014, <http://ethos.bl.uk/OrderDetails.do?uin=uk.bl.ethos.627853>.
- [15] S. Courrech du Pont, P. Gondret, B. Perrin, M. Rabaud, Granular Avalanches in Fluids, *Phys. Rev. Lett.* 90 (4), 044301, <https://doi.org/10.1103/PhysRevLett.90.044301>.
- [16] C. Cassar, M. Nicolas, O. Pouliquen, Submarine granular flows down inclined planes, *Phys. Fluids* 17 (10) (2005) 103301, <https://doi.org/10.1063/1.2069864>.
- [17] F. Boyer, . Guazzelli, O. Pouliquen, unifying suspension and granular rheology, *Phys. Rev. Lett.* 107 (18), 188301, <https://doi.org/10.1103/PhysRevLett.107.188301>.
- [18] L. Amarsid, J.-Y. Delenne, P. Mutabaruka, Y. Monerie, F. Perales, F. Radjai, Viscoplastic regime of immersed granular flows, *Phys. Rev. E* 96 (1), 012901, <https://doi.org/10.1103/PhysRevE.96.012901>.
- [19] F. da Cruz, S. Emam, M. Prochnow, J.-N. Roux, F. Chevoir, Rheophysics of dense granular materials: discrete simulation of plane shear flows, *Phys. Rev. E Stat. Nonlinear Soft Matter Phys.* 72 (2005) 021309.
- [20] P. Jop, Y. Forterre, O. Pouliquen, A constitutive law for dense granular flows, *Nature* 441 (7094) (2006) 727–730, <https://doi.org/10.1038/nature04801>.
- [21] A. Bougouin, L. Lacaze, Granular collapse in a fluid: different flow regimes for an initially dense-packing, *Phys. Rev. Fluids* 3 (6) (2018) 064305, <https://doi.org/10.1103/PhysRevFluids.3.064305>.
- [22] Y.D. Sobral, T.F. Oliveira, F.R. Cunha, On the unsteady forces during the motion of a sedimenting particle, *Powder Technol.* 178 (2) (2007) 129–141, <https://doi.org/10.1016/j.powtec.2007.04.012>.
- [23] T. Zhao, G.T. Houlsby, S. Utili, Investigation of granular batch sedimentation via DEMCFD coupling, *Granul. Matter* 16 (6) (2014) 921–932, <https://doi.org/10.1007/s10035-014-0534-0>.
- [24] G.K. Batchelor, *An Introduction to Fluid Dynamics*, Cambridge University Press, Cambridge, U.K., New York, NY, 2000.
- [25] R. Di Felice, The voidage function for fluid-particle interaction systems, *Int. J. Multiphase Flow* 20 (1) (1994) 153–159, [https://doi.org/10.1016/0301-9322\(94\)90011-6](https://doi.org/10.1016/0301-9322(94)90011-6).
- [26] J. Shafer, S. Dippel, D.E. Wolf, Force Schemes in Simulations of Granular Materials, *Journal de Physique I* 6 (1) (1996) 5–20, <https://doi.org/10.1051/jp1:1996129>.
- [27] S. Luding, Cohesive, frictional powders: contact models for tension, *Granul. Matter* 10 (4) (2008) 235–246, <https://doi.org/10.1007/s10035-008-0099-x>.
- [28] N.V. Brilliantov, F. Spahn, J.-M. Hertzsch, T. Poschel, Model for collisions in granular gases, *Phys. Rev. E* 53 (5) (1996) 5382–5392, <https://doi.org/10.1103/PhysRevE.53.5382>.
- [29] L.E. Silbert, D. Erta, G.S. Grest, T.C. Halsey, D. Levine, S.J. Plimpton, Granular flow down an inclined plane: Bagnold scaling and rheology, *Phys. Rev. E* 64 (5) (2001) 051302, <https://doi.org/10.1103/PhysRevE.64.051302>.
- [30] DCS Computing GmbH, JKU Linz, Sandia Corporation, The Gran-Model-Hertz Model in LIGGGHTS v3.X Documentation, https://www.cfdem.com/media/DEM/docu/gran_model_hertz.html 2016.
- [31] T. Poschel, C. Saluena, T. Schwager, Scaling properties of granular materials, *Phys. Rev. E* 64 (1), 011308, <https://doi.org/10.1103/PhysRevE.64.011308>.
- [32] L. Jing, C.Y. Kwok, Y.F. Leung, Y.D. Sobral, Extended CFD-DEM for free-surface flow with multi-size granules: CFD-DEM for Free-Surface Flow, *Int. J. Numer. Anal. Methods Geomech.* 40 (1) (2016) 62–79, <https://doi.org/10.1002/nag.2387>.
- [33] L. Jing, C.Y. Kwok, Y.F. Leung, Y.D. Sobral, Characterization of base roughness for granular chute flows, *Phys. Rev. E* 94 (5) (2016), 052901, <https://doi.org/10.1103/PhysRevE.94.052901>.
- [34] C. Kloss, C. Goniva, A. Hager, S. Amberger, S. Pirker, Models, algorithms and validation for opensource DEM and CFDDM, *Prog. Comput. Fluid Dyn. Int. J.* 12 (2) (2012) 140–152, <https://doi.org/10.1504/PCFD.2012.047457>.
- [35] R. Zenit, Computer simulations of the collapse of a granular column, *Phys. Fluids* 17 (3) (2005), 031703, <https://doi.org/10.1063/1.1862240>.
- [36] L. Staron, E.J. Hinch, The spreading of a granular mass: role of grain properties and initial conditions, *Granul. Matter* 9 (3–4) (2007) 205–217, <https://doi.org/10.1007/s10035-006-0033-z>.
- [37] L. Lacaze, R. R. Kerswell, Axisymmetric granular collapse: a transient 3d flow test of viscoplasticity, *Phys. Rev. Lett.* 102 (10), 108305, <https://doi.org/10.1103/PhysRevLett.102.108305>.
- [38] L. Girolami, V. Hergault, G. Vinay, A. Wachs, A three-dimensional discrete-grain model for the simulation of dam-break rectangular collapses: comparison between numerical results and experiments, *Granul. Matter* 14 (3) (2012) 381–392, <https://doi.org/10.1007/s10035-012-0342-3>.
- [39] S. Utili, T. Zhao, G. Houlsby, 3d DEM investigation of granular column collapse: Evaluation of debris motion and its destructive power, *Eng. Geol.* 186 (2015) 3–16, <https://doi.org/10.1016/j.enggeo.2014.08.018>.
- [40] X. Li, J. Zhao, Dam-break of mixtures consisting of non-Newtonian liquids and granular particles, *Powder Technol.* 338 (2018) 493–505, <https://doi.org/10.1016/j.powtec.2018.07.021>.
- [41] OpenCFD, OpenFOAM - The Open Source Computational Fluid Dynamics (CFD) Toolbox, <http://www.openfoam.com> 2016.
- [42] T.B. Anderson, R. Jackson, Fluid mechanical description of fluidized beds. Equations of motion, *Ind. Eng. Chem. Fundam.* 6 (4) (1967) 527–539, <https://doi.org/10.1021/i160024a007>.
- [43] Y. Tsuji, T. Kawaguchi, T. Tanaka, Discrete particle simulation of two-dimensional fluidized bed, *Powder Technol.* 77 (1) (1993) 79–87, <http://www.sciencedirect.com/science/article/pii/0032591093850107>.
- [44] S. Bharathraj, V. Kumaran, Effect of particle stiffness on contact dynamics and rheology in a dense granular flow, *Phys. Rev. E* 97 (1), 012902, <https://doi.org/10.1103/PhysRevE.97.012902>.
- [45] A. Singh, V. Magnanimo, K. Saitoh, S. Luding, The role of gravity or pressure and contact stiffness in granular rheology, *New J. Phys.* 17 (4) (2015) 043028, <https://doi.org/10.1088/1367-2630/17/4/043028>.